

Phase retrieval for Bragg coherent diffraction imaging at high x-ray energies

S. Maddali, Marc Allain, W. Cha, R. Harder, S. Park, P. Kenesei, J. Almer, Y. Nashed, S. Hruszkewycz

▶ **To cite this version:**

S. Maddali, Marc Allain, W. Cha, R. Harder, S. Park, et al.. Phase retrieval for Bragg coherent diffraction imaging at high x-ray energies. Physical Review A : Atomic, molecular, and optical physics [1990-2015], 2019, 99 (5), pp.053838. 10.1103/PhysRevA.99.053838 . hal-02139472

HAL Id: hal-02139472
https://amu.hal.science/hal-02139472

Submitted on 24 May 2019

HAL is a multi-disciplinary open access archive for the deposit and dissemination of scientific research documents, whether they are published or not. The documents may come from teaching and research institutions in France or abroad, or from public or private research centers.

L'archive ouverte pluridisciplinaire **HAL**, est destinée au dépôt et à la diffusion de documents scientifiques de niveau recherche, publiés ou non, émanant des établissements d'enseignement et de recherche français ou étrangers, des laboratoires publics ou privés.



Distributed under a Creative Commons Attribution 4.0 International License

Phase retrieval for Bragg coherent diffraction imaging at high x-ray energies

S. Maddali,[1,*] M. Allain,[2] W. Cha,[3] R. Harder,[3] J.-S. Park,[3] P. Kenesei,[3] J. Almer,[3] Y. Nashed,[4] and S. O. Hruszkewycz[1]

[1]*Materials Science Division, Argonne National Laboratory, Lemont, Illinois 60439, USA*

[2]*Aix Marseille Univ, CNRS, Centrale Marseille, Institut Fresnel, Marseille, France*

[3]*X-ray Sciences Division, Argonne National Laboratory, Lemont, Illinois 60439, USA*

[4]*Mathematics and Computer Science Division, Argonne National Laboratory, Lemont, Illinois 60439, USA*

(Received 16 November 2018; published 23 May 2019)

Coherent x-ray beams with energies $\geqslant 50$ keV can potentially enable three-dimensional imaging of atomic lattice distortion fields within individual crystallites in bulk polycrystalline materials through Bragg coherent diffraction imaging (BCDI). However, the undersampling of the diffraction signal due to Fourier-space compression at high x-ray energies renders conventional phase-retrieval algorithms unsuitable for three-dimensional reconstruction. To address this problem, we utilize a phase-retrieval method with a Fourier constraint specifically tailored for undersampled diffraction data measured with coarse-pitched detector pixels that bin the underlying signal. With our approach, we show that it is possible to reconstruct three-dimensional strained crystallites from an undersampled Bragg diffraction data set subject to pixel-area integration without having to physically upsample the diffraction signal. Using simulations and experimental results, we demonstrate that explicit modeling of Fourier-space compression during phase retrieval provides a viable means by which to invert high-energy BCDI data, which is otherwise intractable.

DOI: 10.1103/PhysRevA.99.053838

I. INTRODUCTION

Coherent diffraction imaging (CDI) with radiation in the lower end of the hard x-ray range ($\sim$10 keV) is steadily gaining traction as a technique for imaging objects ranging in size from tens of micrometers to tens of nanometers with sensitivity to diverse physical properties. For example, when applied to Bragg reflections from single crystals, CDI and related techniques such as ptychography are capable of spatial mapping of lattice imperfections such as strain and crystal defects [1–5], thus providing a versatile tool applicable in materials science and solid-state physics. In particular, Bragg CDI (BCDI) at x-ray energies $\geqslant 50$ keV can potentially allow the probing of nanoscale structural detail within crystalline grains of a much-larger-scale bulk material. This is possible due to the greater penetrative power at these photon energies compared to those in present-day measurements, owing to greatly diminished absorption and extinction effects [6]. Though other high-energy x-ray methods have been developed that do not rely on beam coherence to achieve micrometer-scale resolution of grains in bulk materials (e.g., diffraction contrast tomography and high-energy diffraction microscopy [7–9]), implementation of high-energy BCDI has not been viable due to low coherent flux at high x-ray energies at today's synchrotron facilities. Fortunately, improvements in synchrotron storage ring technology [10] now being adopted around the world will enable greatly increased coherent flux at energies greater than 50 keV, making high-energy CDI practical in the near future. This in turn would open up an entirely new class of possible experiments for three-dimensional high-resolution strain field mapping at such light sources. Specific systems of interest include individual grains embedded in bulk polycrystals subject to real-world thermomechanical conditions, and crystals embedded in other dense media to mimic, for example, catalytic environments. However, in envisioning such BCDI experiments, certain difficulties can be foreseen from the standpoint of signal processing and image inversion.

Successful reconstruction of the image of a diffracting crystallite from a BCDI measurement is predicated upon sufficient resolution of the signal features (fringe distribution about a Bragg peak). In any CDI experiment performed at high x-ray energies, compression of the three-dimensional Fourier space will directly impact the ability to satisfy this condition, given the fixed sizes of typical area detector pixels and practically realizable object-detector distances. Existing methods seek to address this issue through initial signal processing by combining physical upsampling and sparsity-based methods [11,12] to arrive at postprocessed diffraction patterns suitable for conventional phase-retrieval methods. In the same spirit, a recent simulation work [13] demonstrates the possibility of BCDI signal enhancement with refractive optical elements prior to phase retrieval. In this article, we implement a direct phase-retrieval solution for undersampled BCDI data sets from compact single crystals, an approach directly applicable to future studies of embedded crystals. Our explicit modeling of Fourier-space compression is related conceptually to an earlier work in transmission ptychography [14], in which binning-induced resolution loss due to coarse pixelation is offset by information redundancy through a high degree of probe position overlap. Our CDI-specific work similarly focuses on phase retrieval from undersampled signals, but without incorporating signal redundancy, as in ptychography. We precisely quantify the extent to which

*smaddali@anl.gov

 ©2019 American Physical Society

modeling of Fourier-space compression alone allows us to relax signal sampling requirements to obtain reconstructions free of binning artifacts [15]. Our work in this article (i) alludes to a fundamental theoretical limit in binning-related signal-processing applications that allows us to partially relax the well-known Nyquist criterion for CDI experiments and, in addition, (ii) provides an inexpensive alternative to constructing large experimental enclosures to enable sufficient angular resolution at high beam energies. This limit comprises a more permissive sampling criterion for successful image reconstruction, and is afforded by the additional constraints imposed on the data through modeling the compression of Fourier space during phase retrieval. While our focus in this article is on BCDI measurements and the reconstruction of complex three-dimensional objects, the methods described here can also be adapted to two-dimensional transmission CDI measurements.

The outline of this article is as follows: in Sec. II, we describe the effect of Fourier-space compression on a BCDI signal and the phase-retrieval framework that explicitly models this. In Sec. III, we present the three-dimensional reconstructions from simulated high-energy scattering as well as a reconstruction from an experimental Bragg coherent diffraction measurement designed to emulate high beam energy. We also discuss the limits of binning for successful phase retrieval and derive the resultant sampling criterion. In Sec. IV, we discuss the potential ramifications of this method for the design of high-energy CDI experiments.

II. PHASE RETRIEVAL WITH FOURIER-SPACE COMPRESSION

In a BCDI measurement, a compact single crystal coherently illuminated with monochromatic x rays is rotated through the Bragg condition in small angular steps (typically 0.01° steps over a 0.5° range for a 9 keV energy beam). The three-dimensional scattered intensity is queried with such a scan in a sequence of parallel slices, as shown in Fig. 1(a).

For a given Bragg reflection, the beam energy E is inversely proportional to the Bragg angle θ_{Bragg}. Also since $|\boldsymbol{q}| = |\boldsymbol{k}_f - \boldsymbol{k}_i| \propto 2\sin\theta_{\text{Bragg}}$, the scale of Fourier space is inversely proportional to E. The fringe spacing and angular extents of the diffraction patterns resulting from energies αE and E are in the ratio $1/\alpha^2$ for some multiplicative factor α. Consequently, the same Fourier-space aperture is resolved by proportionately fewer pixels at higher beam energies (i.e., when $\alpha > 1$), as seen in Fig. 1(b). The effect of this compression on the measured signal is modeled by binning the well-resolved diffraction pattern into proportionately larger pixels, and for this reason we call α the pixel binning factor (PBF). Figure 2(e) shows the kth binned intensity pattern $\mathbf{I}_k \in \mathbb{R}^{M\times M}$ from a sequence of diffraction images $\mathbf{I} = \{\mathbf{I}_k | k = 1, 2, \ldots, K\}$ acquired in a high-energy BCDI experiment.

This signal (noisy in practice) is related to a virtual, high-resolution image $\mathbf{I}_k^{\uparrow} \in \mathbb{R}^{N\times N}$(with $N > M$) that is not accessed experimentally,

$$\langle I_{\mu\nu;k}\rangle = \epsilon_{\mu\nu;k} + \sum_{i,j\in B_{\mu\nu;k}} I^{\uparrow}_{ij;k}, \tag{1}$$

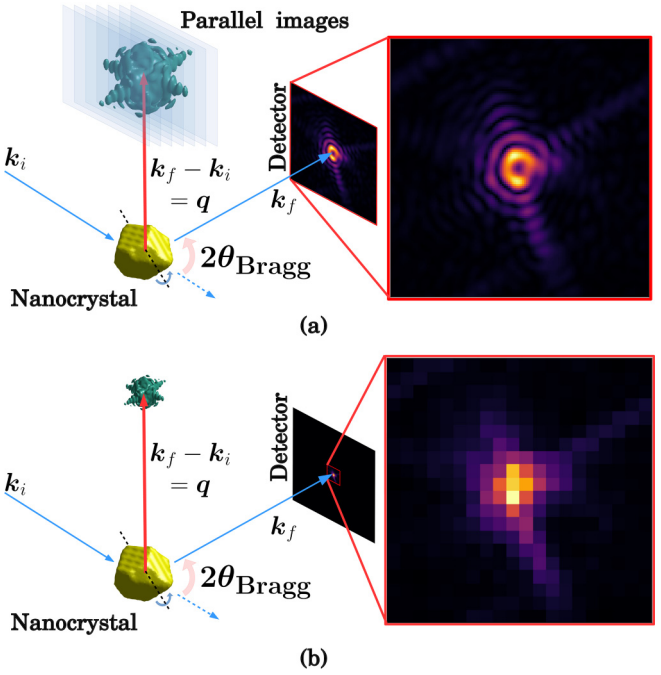


FIG. 1. (a) Schematic of a conventional BCDI experiment resulting in well-sampled fringes. (b) The identical experimental geometry with photon energy that is six times higher, showing the compression of Fourier space and the signal undersampling. $\boldsymbol{k}_i$ and $\boldsymbol{k}_f$ are the incident and scattered wave vectors, respectively, and satisfy $|\boldsymbol{k}_i| = |\boldsymbol{k}_f|$. In these schematics, we compare, side by side, the effects of pixel binning by considering the energy scaling factor alone and, for the sake of simplicity, do not take into consideration the significant reduction in the Bragg angle θ_{Bragg} at six times the original beam energy.

where $\langle\cdot\rangle$ denotes the expectation value. Throughout this article, we use "noisy" to refer to Poisson noise since this is the dominant source of error in the photon counts of a physical BCDI measurement with sufficiently high signal-to-noise ratio. Here, $I_{\mu\nu;k}$ and $I^{\uparrow}_{ij;k}$ are the (μ, ν)th and (i, j)th pixels in $\mathbf{I}_k$ and $\mathbf{I}_k^{\uparrow}$, respectively, and $\epsilon_{\mu\nu;k}$ is the contribution of the incoherent background scattering, which is generally nonzero in x-ray scattering experiments. The index set $B_{\mu\nu;k}$ is a contiguous block of fine pixels in the virtual image $\mathbf{I}_k^{\uparrow}$ that subtends the same solid angle as the measured pixel $I_{\mu\nu;k}$ [Fig. 2(c)]. This model intentionally does not account for compression along the third independent direction k owing to the availability of high-resolution rotation stages (rotational precision $\sim 0.0003^\circ$) at coherent scattering facilities that can accommodate the compression of Fourier space along k by simply reducing the angular step size of a scan. Further, since the radius of curvature of the Ewald sphere is proportional to the beam energy, the effects of this curvature are even more diminished at $\geqslant 50$ keV than at typical CDI energies of ~ 8 keV. For this reason, we focus on the issue of detector-plane binning alone.

We note that in general, the introduction of $\epsilon_{\mu\nu;k}$ in Eq. (1) introduces significant complexity into the analysis of the acquired signal. A relatively strong $\boldsymbol{q}$-dependent incoherent background would render it difficult at best to infer the true

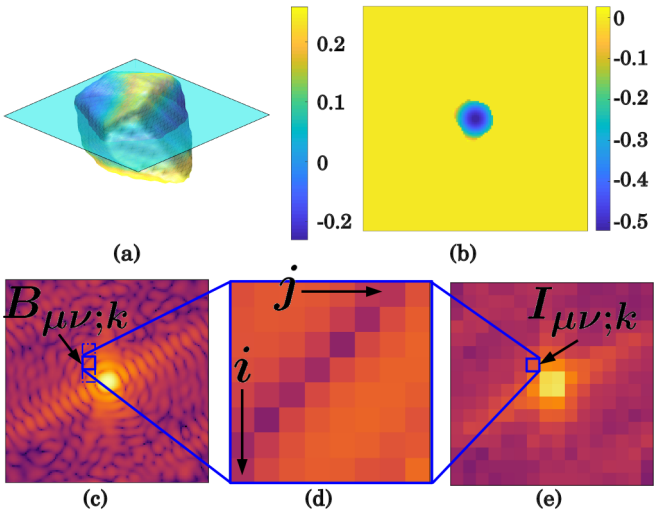


FIG. 2. (a) A simulated complex-valued 3D object (128 × 128 × 70 pixels) with surface phases, with the color scale in units of radians. (b) A 128 × 128-pixel slice depicting the phase through the middle of the object in (a). (c) High-resolution diffraction pattern representing the kth 2D slice of the 3D intensity pattern (in simulated photon counts) corresponding to the object in (a). A contiguous 8 × 8 block in this pattern is indexed by (μ, ν), along with neighboring blocks $(\mu \pm 1, \nu)$. (d) Zoom-in of the block in (c). (e) Binned diffraction pattern (16 × 16) showing a pixel whose intensity is the sum of those in the block $B_{\mu\nu k}$.

contribution from the coherently diffracting object. However, a relatively low-level incoherent background superposed on an otherwise high-quality BCDI signal can be addressed with a simple background subtraction, as is common practice. For this reason, we restrict ourselves in this article to theoretical analysis and simulations in which $\epsilon_{\mu\nu;k} = 0$, and apply a simple background subtraction to the experimental data in Sec. III C.

The wave field $\boldsymbol{\psi}_k \in \mathbb{C}^{N\times N}$ associated with each $\mathbf{I}_k^{\uparrow}$ satisfies

$$\mathbf{I}_k^{\uparrow} = |\boldsymbol{\psi}_k|^2. \tag{2}$$

In the Fraunhofer regime [16], these quantities are related to the unknown compact, three-dimensional, complex-valued scatterer $\boldsymbol{\rho}$ through the discrete three-dimensional (3D) Fourier transform operator $\mathcal{F}_{3D}$,

$$\boldsymbol{\psi} = \mathcal{F}_{3D}[\boldsymbol{\rho}], \tag{3}$$

where $\boldsymbol{\psi} \in \mathbb{C}^{N\times N\times K}$ is the array built from sequential, parallel, 2D slices of the diffracted field $\boldsymbol{\psi}_k$. Our goal is to design a phase-retrieval algorithm that reconstructs the well-resolved quantities $\boldsymbol{\rho}$ and $\boldsymbol{\psi}$ by explicitly capturing the binning [(1)–(3)]. In particular, we utilize the following Fourier-space constraint (first introduced in Ref. [14] in the context of ptychography) to update $\psi_{ij;k}^{(n)}$ at iteration n:

$$\psi_{lm;k}^{(n+1)} = \left[\frac{I_{\mu\nu;k}}{\sum\limits_{i,j\in B_{\mu\nu;k}} \left|\psi_{ij;k}^{(n)}\right|^2}\right]^{\frac{1}{2}} \psi_{lm;k}^{(n)} \quad \forall\, l,m \in B_{\mu\nu;k}. \tag{4}$$

This update operation ensures that the estimated 3D diffracted field $\boldsymbol{\psi}^{(n)}$ at each iteration n is consistent with the binning model defined in Eq. (1). Equation (4) results in modified versions of the commonly used iterative algorithms in phase-retrieval recipes (of which Ref. [17] contains a comprehensive review). Of these, we use the Gerchberg-Saxton error reduction (ER) [18] and Fienup's hybrid input-output (HIO) [1] for the reconstructions in this article. The object support is periodically updated using a "shrinkwrap" algorithm [19].

This manner of Fourier-space signal binning shares a strong similarity with a ptychographic fly-scan measurement in real space, described in a recent article [20]. In this fly-scan work, the acquired signal is modeled as the aggregate of intensity contributions from discrete probe positions in the fly-scan path. The resolution loss as a function of increasing scanning speed described in this fly-scan work is analogous to the case of CDI in the presence of Fourier-space compression, where we expect degradation of the final image quality from phase retrieval as a function of increased binning. We investigate this trend comprehensively in Sec. III.

Equation (4) is also derived from a robust Gaussian model of the photon-counting process [21,22]; see Appendix A for a detailed derivation. This ensures that our update (4) is consistent with a statistically sound inference method with good asymptotic properties [22].

Lastly, we note that at beam energies $\geqslant$ 50 keV, there is negligible crosstalk between successive acquired images in a BCDI measurement owing to the near orthogonality of the discrete sampling directions in Fourier space (see Appendix B for details). This effectively brings the high-energy versions of BCDI and transmission CDI on the same footing and allows us to describe our method in terms of the more general three-dimensional BCDI, with two-dimensional transmission CDI being a special case. At lower beam energies, a substantial skew in the Fourier-space sampling directions results in non-negligible crosstalk between successive images and might provide BCDI with an advantage over transmission CDI in terms of the stability of such a phase-retrieval algorithm.

III. RESULTS

A. Reconstructions from simulated scattering

For simulation purposes, a synthetic complex-valued object $\boldsymbol{\rho}$ with arbitrarily oriented facets was created within a three-dimensional complex array to represent a nanoscale crystalline particle with a definite strain state. Pixels within the particle were assigned an amplitude of 1, and phase values that varied continuously and gradually in three dimensions. The phase for each simulated crystal was chosen to vary as a multivariate Gaussian centered on the middle of the numerical array and whose standard deviation was comparable to the size of the particle, as can be seen from the cross section in Fig. 2(b). Pixels outside the particle were set to 0. The corresponding far-field scattering signal was determined from the 3D Fourier transform: $\mathbf{I}^{\uparrow} = |\mathcal{F}_{3D}[\boldsymbol{\rho}]|^2$. Sufficient oversampling of the diffraction fringes in $\mathbf{I}^{\uparrow}$ was ensured by providing a buffer of zero-valued pixels around the particle such that the particle size was below one-third of the array size in each dimension. This ensured that the autocorrelation $\boldsymbol{\rho} \otimes \boldsymbol{\rho}$

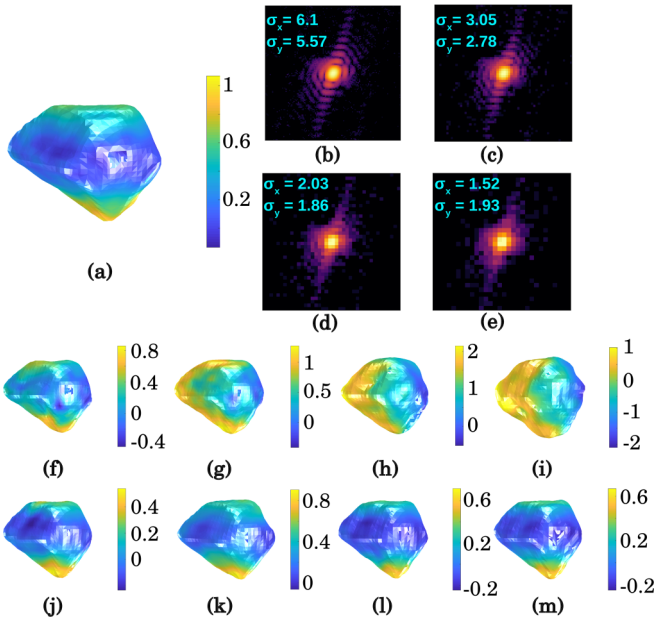


FIG. 3. (a) Isosurface plot of a synthetic particle reconstructed with conventional phase retrieval ($\alpha = 1$), which we use as a ground truth for comparison. (b)–(e) Central slices through binned diffraction signals (simulated photon counts) for $\alpha = 2, 4, 6, 8$, respectively, with steadily degrading fringe visibility (including sampling rates σ_x, σ_y along the axes of the imaging plane). (f)–(i) Isosurface plots of synthetic particles recovered using conventional phase retrieval on binned noisy signals with $\alpha = 2, 4, 6, 8$. (j)–(m) Isosurface plots of synthetic particles recovered using modified phase retrieval on binned noisy signals with $\alpha = 2, 4, 6, 8$ show much better agreement with (a). All the color bars denote the phase expressed in radians. The pixelation in the final reconstructions was removed by Gaussian kernel smoothing and the isosurfaces were plotted at a value of 0.5 of the maximum object amplitude.

was fully contained in the simulation array, preventing cyclic aliasing. In our constructions, the particle and grid sizes were chosen to give a sampling rate (defined as $\sigma \equiv N/s$, where N and s are the pixel spans of the array and particle, respectively) well above the Nyquist rate of $\sigma = 2$ in each dimension. For various choices of the pixel binning factor α, higher-energy diffraction patterns were simulated by binning the intensities $I^{\uparrow}_{ij;k}$ in the first two dimensions into pixel blocks of size α^2 to obtain $\mathbf{I}_k$, after which Poisson noise was added to simulate a physical measurement. The values of α were chosen to demonstrate progressive loss of fringe visibility. Post binning, the pixels on the edges of the array that were not incorporated into any of the bins $B_{\mu\nu;k}$ were discarded. Thus, in each case, the original object was recovered on a numerical grid of size $\alpha N_\alpha \times \alpha N_\alpha \times 70$, where N_α was the detector-plane pixel span of the binned intensity $\mathbf{I}_k$. The signal strength was chosen to give a signal-to-noise ratio (SNR) of ∼40 dB in the vicinity of the Bragg peak. This corresponds to an approximate photon count of 30 000 at the Bragg peak, similar to those in typical BCDI measurements [23,24].

A systematic comparison of modified and conventional phase-retrieval schemes as a function of fringe visibility is shown in Fig. 3. A synthetic object of pixel span $\simeq$ 25 contained in a $256 \times 256 \times 70$-pixel array was used, resulting in sampling rates of $\boldsymbol{\sigma} = (\sigma_x, \sigma_y) = (12.19, 11.13)$ in orthogonal directions in the detector plane and 3.03 in the third direction. Figures 3(b)–3(e) show a pronounced loss of fringe visibility as the degree of binning increases. As a result, the conventional phase-retrieval approach that does not account for binning results in lower-quality reconstructions [Figs. 3(f)–3(i)]. In contrast, accounting for Fourier-space compression gives the reconstructions in Figs. 3(j)–3(m), which more accurately reproduce the morphology and phase features of the reconstruction of the unbinned ($\alpha = 1$) data set, which was obtained using unmodified ER and HIO algorithms [Fig. 3(a)]. Figure 4 shows cross sections of the amplitudes and phases of the reconstructions seen in Fig. 3. Repetitions of the modified phase-retrieval recipe with different random initial values for $\boldsymbol{\rho}$ were found to repeatedly converge to very similar solutions, one set of which are shown in this figure. A Gaussian filter of sufficiently small kernel width (three pixels) was applied to these reconstructions in order to obtain the smooth isosurfaces seen in Fig. 3. In addition to Gaussian filtering, a variety of methods may be employed to refine the reconstructions obtained from a single run of the phase-retrieval recipe, such as averaging the reconstructions from different randomized initializations, phase-retrieval genetic algorithms [25], or incorporating upsampled signal information into the modified phase retrieval, obtained by translating the area detector across the exit beam in subpixel steps [11].

We note that the binned diffraction patterns corresponding to $\alpha = 2, 4$ yielded sampling rates of $\sigma \simeq 6, 3$, respectively, both of which are well above the Nyquist sampling threshold of 2. In these cases, we would expect that the unmodified phase-retrieval approach would be appropriate for these data and that the modified phase retrieval would not improve the image significantly. However, in our numerical tests, we see that this is not the case: the images in Figs. 3(f) and 3(g) (unmodified algorithm) do not reproduce the phase features of Fig. 3(a) as well as Figs. 3(j) and 3(k), even though the morphology is reproduced faithfully. This is because of the inherent difference between binning and sampling in a strict signal-processing sense. Aggregation of the continuous intensity field (i.e., binning) in each pixel block $B_{\mu\nu;k}$ of a high-resolution diffraction pattern is a mathematical transformation that is fundamentally different from collecting a set of periodically spaced points from the high-resolution pattern (i.e., periodic sampling) [26]. It is only to the latter that the Nyquist criterion strictly applies, even though the terms "undersampling" and "overbinning" are sometimes used interchangeably in the context of solid angles subtended by a pixel. The effects of this difference, as our tests show, are prominent at sampling rates near 2. However, the binning model we have introduced can be applied in such circumstances to mitigate these artifacts.

B. Limits of pixel binning

We now address the limits of the user-defined binning (or, equivalently, upsampling) parameter α for successful phase retrieval given a binned CDI data set. For the purposes of this discussion, we consider this effect in terms of a single oversampled image $\mathbf{I}^{\uparrow(2D)}$ from a sequence of images [Fig. 5(a)]

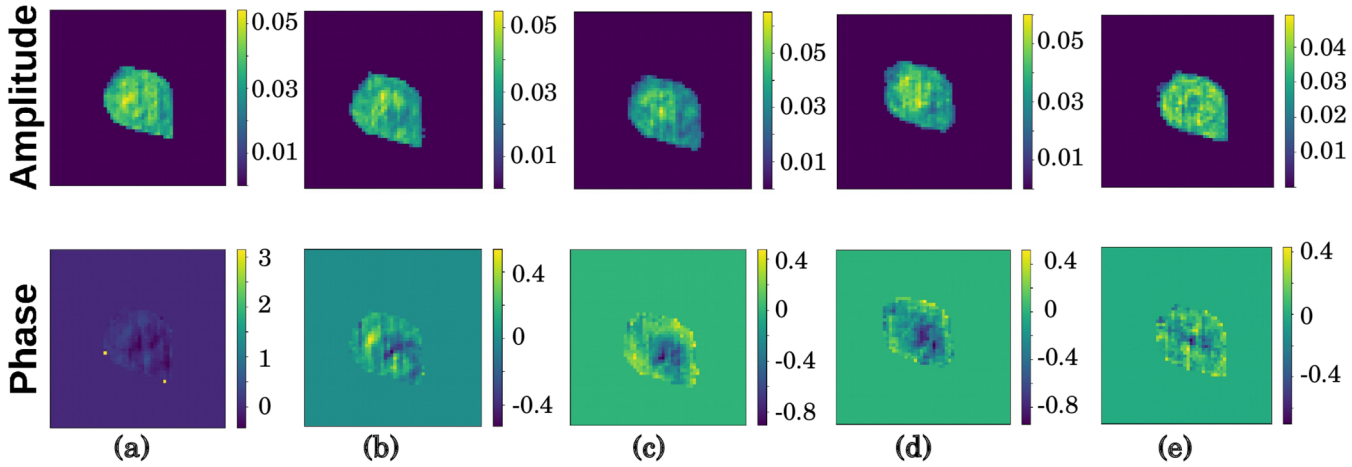


FIG. 4. (a) Amplitude and phase cross sections of the reconstructed crystal shown in Fig. 3(a), from conventional phase retrieval applied to unbinned diffraction (prior to Gaussian filtering). (b)–(e) Slices from the reconstructions corresponding to $\alpha = 2, 4, 6, 8$. The amplitude is expressed in arbitrary units, while the phase is expressed in radians. The central dip in the phase is discernible in all reconstructions.

without loss of generality. We frame the analysis below by interpreting the binning operator in terms of a convolution kernel.

The pixel intensities obtained by two-dimensional binning of $\mathbf{I}^{\uparrow(2D)}$ can be thought of as periodically sampled from the 2D convolution of the oversampled intensity pattern and a 2D box function: $\mathbf{I}^{\uparrow(2D)} * \mathbf{W}$. The convolution kernel $\mathbf{W}$ is a square window of size $\alpha \times \alpha$ pixels whose Fourier transform is the 2D sinc function [Fig. 5(b)]. Further, it is known that the 2D Fourier representation of $\mathbf{I}^{\uparrow(2D)}$ is compact (see the Supplemental Material of Ref. [12]). We show here that the Fourier representation of $\mathbf{I}^{\uparrow(2D)} * \mathbf{W}$ (i.e., the product of the respective 2D Fourier transforms) is indicative of the threshold of irreversible information loss. We use $\mathcal{F}_{2D}[\cdot]$ to denote the 2D Fourier transform operator.

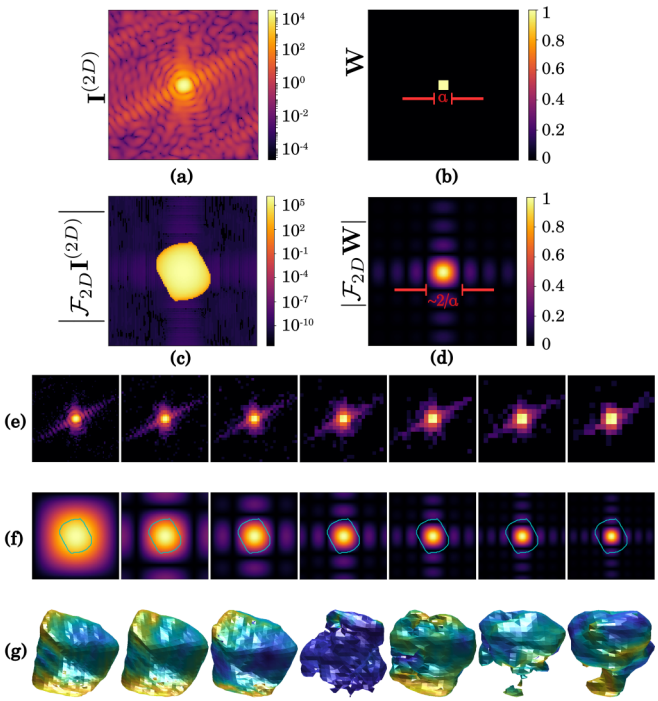


FIG. 5. (a) Single detector image. (b) Convolution kernel corresponding to binning operation. (c) Fourier transform of the detector image (Patterson function), also equal to the object autocorrelation $\boldsymbol{\rho} \otimes \boldsymbol{\rho}$, projected in the imaging plane. (d) 2D sinc function which is the Fourier transform of the convolution kernel in (b). (e) Sequence of central slices of noisy signals corresponding to $\alpha = 2$ through 8. (f) Fourier-space representations of the corresponding convolution kernels overlaid with the outline of the Patterson function. (g) Reconstructions from the modified phase-retrieval method indicating degradation of image quality from $\alpha = 5$ onwards.

The sequences of images in Figs. 5(e)–5(g) correspond to increasingly large binning windows ($\alpha = 2$ through 8), applied to a different (arbitrarily faceted) simulated nanocrystal, similar to the one featured in Fig. 3. In the corresponding Fourier representation [Figs. 5(f)], we see that signal information is lost when any significant component of the compact function $\mathcal{F}_{2D}\mathbf{I}^{\uparrow(2D)}$ is suppressed to zero through multiplication with $\mathcal{F}_{2D}\mathbf{W}$. This situation occurs at the nodes of the function $\mathcal{F}_{2D}\mathbf{W}$, for $\alpha > 4$. Thus the criterion for successful phase retrieval is that $\mathcal{F}_{2D}\mathbf{I}^{\uparrow(2D)}$ should lie entirely within the central lobe of $\mathcal{F}_{2D}\mathbf{W}$. This limit is clearly demonstrated in Fig. 5(g), wherein the quality of 3D image reconstruction suffers dramatically when α is too high for the given particle. An experimental ramification to this limit is that, for a fixed experimental geometry (x-ray energy, object-detector distance, detector pixel size), the largest value of α one can choose for phase retrieval is limited by the scatterer size.

We now cast the above criterion in the perspective of a physical BCDI measurement. In particular, we show that the criterion results in a relaxation by a factor of 2 in the maximum size of the scatterer as permitted by the Nyquist condition, which is usually adhered to in CDI experiments. Consider the relation between the Fourier-space size of a single detector pixel Δq and the experimental parameters such as the physical pixel size p, sample-detector distance z, and the beam energy E: $\Delta q = Ep/hcz$, where h is Planck's constant and c is the speed of the propagating wave [16]. If x_0 is the largest span of the real-space scatterer, then the Nyquist criterion dictates that $\Delta q \leqslant 1/(2x_0)$ for sufficient sampling of diffraction fringes and therefore successful (unmodified)

phase retrieval. This gives the criterion for the maximum permissible scatterer size for a given experimental configuration,

$$x_0 \leqslant \left(\frac{1}{2}\right)\frac{hcz}{Ep}. \tag{5}$$

The criterion derived earlier in this section, on the other hand, dictates that the span of $\mathcal{F}_{2D}\mathbf{I}^{\uparrow(2D)}$ (equal to $2x_0$ in real-space units) should be no larger than the size of the central lobe of the sinc function corresponding to the single pixel window in Fourier space (equal to $2/\Delta q$ in the same real-space units). This gives us a new scatterer-size criterion,

$$x_0 \leqslant \frac{hcz}{Ep}, \tag{6}$$

which represents a factor of 2 relaxation in the Nyquist bound of (5). If the scatterer is larger than the threshold in (6), the modified phase-retrieval method presented in this work will fail without the acquisition of additional signal data (for example, as described in Refs. [11,12]), or modification of the experiment itself. Beyond such modifications to the BCDI setup, the imaging of extended structures well beyond this size threshold by using focused high-energy x rays (i.e., high-energy ptychography) is currently an active area of research [27].

It may appear that the BCDI phase-retrieval problem with Fourier-space scaling is inherently underdetermined because the unknowns in the discrete quantity $\boldsymbol{\rho} \in \mathbb{C}^{N\times N\times N_2}$ outnumber the binned intensity measurements made with coarse pixels. However, it can be shown that the unknowns and constraints are, in fact, equal in number: for a fine pixel grid of size $N \times N \times N_2$, there are $2N^2N_2$ unknowns to solve for, with the factor of 2 arising from the real and imaginary (or, equivalently, amplitude and phase) components of $\boldsymbol{\rho}$. On the other hand, (4) imposes exactly N^2N_2 independent Fourier-space constraints on $\boldsymbol{\rho}$ (since for a general $\rho_{ij;k}$ we have $i, j \in \{1, 2, \ldots, N\}$ and $k \in \{1, 2, \ldots, N_2\}$), while the support constraint imposes another N^2N_2 independent constraints by scalar multiplication of each pixel with either 0 or 1. Even though the unknowns and constraints are equal in number, convergence of the phase retrieval to a unique solution requires that the criterion on x_0 above be satisfied so as to not lose information irretrievably.

In our discussion of Fig. 5, we interpreted the binning transformation of a coherent diffraction pattern as a convolution followed by a uniform sampling operation. From the point of view of information loss, this convolution aspect shares an interesting parallel with the phenomenon of partial coherence in CDI. It has been shown that the scattered intensity field in the presence of partial coherence can be treated as the convolution of the propagated coherent intensity field with a blurring kernel, typically a multivariate Gaussian function at third-generation synchrotrons [24,28,29]. The subsequent deconvolution process to estimate the propagated wave field is computationally simpler and avoids the separate characterization of the synchrotron beam as a superposition of coherent modes [30,31]. This modeling of partially coherent diffraction differs from the binning transformation described above only in the type of convolution kernel used, the latter being a square function as we have already seen. Both of these processes result in reduced fringe visibility, and can be interpreted as a modulation of the autocorrelation of the diffracting object by an envelope function (which is a sinc function for binning). In both cases, the modulating effect of the envelope can be undone to obtain the pristine signal, provided none of its significant components are suppressed by the envelope. However, the binning case fundamentally differs from the convolution-only case in that additional mathematical modeling is required to account for the inherent reduction in the number of measured data (i.e., the pixel intensity counts) and provide signal sampling.

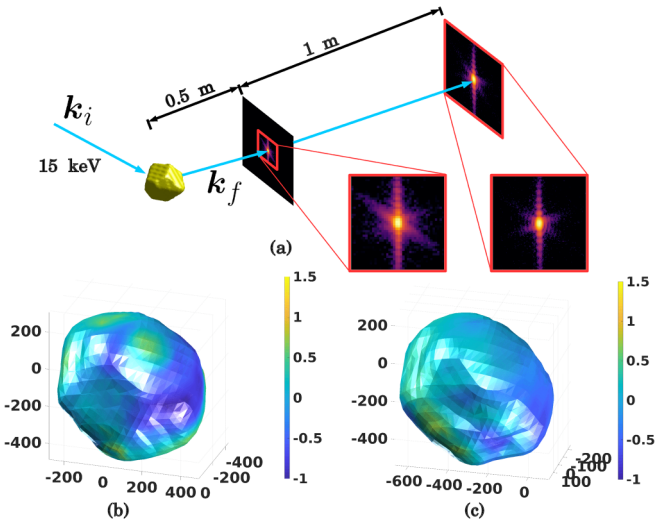


FIG. 6. (a) Experimental schematic for mock high-energy BCDI measurement. (b) Gold nanocrystal from modified phase retrieval acting on signal collected at a distance of 0.5 m [isosurface colored by phase (rad)]. (c) The same nanocrystal from conventional phase retrieval acting on signal collected at 1.5 m. The axis units in (b) and (c) are in nanometers.

C. Experimental validation

To validate our method, we performed a synchrotron experiment in which two 3D BCDI data sets were collected from the same scatterer at the same x-ray beam energy in two different ways: (i) data was measured to ensure highly oversampled fringes appropriate for unmodified BCDI phase retrieval, and (ii) data were measured under "coarse-pixel" conditions wherein the visibility of finely spaced fringes is significantly reduced. In our proof-of-concept experiment, the scatterer used was one of a number of gold nanocrystals of varied sizes obtained by dewetting a gold film on a silicon substrate. The scattering measurements were made at Beamline 34-ID-C of the Advanced Photon Source. A BCDI data set of size $120 \times 120 \times 80$ pixels, appropriate for unmodified phase retrieval, was collected from this particle at a beam energy of 15 keV and an object-detector distance of 1.5 m and an angular step size of 0.005°. The imaged particle resulting from this data set [Fig. 6(b)] was found to be about $400 \times 600 \times 700$ nm in size. The measurement was then repeated with the same beam energy, but with the object-detector separation reduced to one-third of the original distance (i.e., 0.5 m), resulting in significant loss of fringe visibility in the detector plane.

This configuration yields a PBF of $\alpha = 3$ relative to the first measurement because of the 3 : 1 ratio of the object-detector distances. In this sense, such a data set emulates a high-energy BCDI experiment, if one considers a factor of 3 in energy (45 keV) rather than object-detector distance. This avoids the need to perform an actual BCDI experiment at 45 keV with limited x-ray coherence. Further, since the x-ray energy is the same in both cases, the image reconstructions from the two data sets correspond to identical discrete grids in real space. The respective phase-retrieval recipes are given by

(i) Conventional phase retrieval: 900 iterations of ER (shrinkwrap every 30 iterations) → 600 iterations of HIO → 1000 iterations of ER (shrinkwrap every 50 iterations) → 3000 iterations of ER with no intermediate shrinkwrap.

(ii) Modified phase retrieval: 1000 iterations of ER → 2000 iterations of HIO → 1000 iterations of ER → 2000 iterations of HIO → 3000 iterations of ER. Shrinkwrap was applied every 250 iterations during the first 2000 of ER. Prior to this phase retrieval, the background contribution $\epsilon_{\mu\nu;k}$ to the "higher-energy" data set (assumed constant) was artificially dealt with by thresholding the photon counts below 1 to 0.

In general, there is good agreement between the two reconstructions and we speculate that the slight difference in the phase profile between Figs. 6(b) and 6(c) is because of differences in background levels in the two measurements. Namely, physical positioning of the detector closer to the direct beam in the 0.5 m measurement increases the level of air scattering and other background sources.

We caution that while the above experiment emulates most of the essential features of a true 45 keV measurement, there are some salient differences. The first is that the Bragg angle for the two measurements was the same, which would not be the case at 45 keV. This implies non-negligibile crosstalk between successive detector images (see Appendix B). We speculate that the quality of a reconstruction from a true 45 keV measurement would be a little less than the results shown here due to the reduced crosstalk. Second, there was no Fourier-space compression along the rocking direction in the "higher-energy-like" case. This is because the scale of Fourier space depends on the energy of the beam and the relevant lattice plane spacing of the crystal, neither of which changed in moving the detector from 1.5 to 0.5 m. This meant that the same angular step of 0.005° sufficed for both measurements. As mentioned in Sec. II, in a true 45 keV measurement, the compressed Fourier space in the rocking direction can be adequately sampled with high-precision rotation stages.

We also note that because the modified Fourier-space projection of (4) differs from the conventional Fourier-space projection, we expect different rates of convergence, and for this reason we adopted the different phase-retrieval recipes above.

IV. CONCLUSION

We have described a phase-retrieval formalism tailored for undersampled BCDI data from high-energy x-ray scattering measurements that is based upon the modeling of signal binning due to coarse pixelation in Fourier space [14]. The approach we describe is necessitated by the fact that at higher x-ray energies, Fourier-space compression makes it impractical to resolve the fine fringe detail in a coherent diffraction pattern necessary for standard CDI phase-retrieval methods. We have demonstrated with simulations and experiments that phase-retrieval algorithms explicitly designed to take into account the binning effect allow for accurate reconstruction of 3D compact crystals from data that would otherwise be intractable with standard methods. This is possible, to a certain limit, without acquiring any redundant data to serve as constraints, as has been done in related work [11,12,14]. Specifically, we find that our approach enables successful reconstruction of 3D images from coherent diffraction sampled up to a factor of 2 below the Nyquist criterion in the plane of the detector. While we have derived this limit in the context of high-energy BCDI, it could potentially be applicable to a broader class of binning-related digital-imaging applications, depending on the physical origins of the signal.

Within the field of experimental x-ray and materials science, this work has important consequences for the design of space-constrained coherent scattering experiments at high-energy synchrotron facilities. By relaxing the fringe sampling requirements and achieving the desired Fourier-space resolution through algorithmic sophistication, the relatively expensive option of building larger experimental enclosures for high-energy CDI experiments is preempted for a larger range of crystal sizes. Even beam-line facilities with large object-detector distances can benefit from the ability to image larger crystals. While enhancing the flexibility of experimental design, this is also an important step towards facilitating structural imaging experiments of nanoscale crystalline volumes in difficult-to-access environments that require the long penetration depths of high-energy x rays.

ACKNOWLEDGMENTS

Design and simulation of the phase-retrieval framework for high-energy coherent x-ray diffraction was supported by Laboratory Directed Research and Development (LDRD) funding from Argonne National Laboratory, provided by the Director, Office of Science, of the U.S. Department of Energy under Contract No. DE-AC02-06CH11357. Experimental demonstration of the method was supported by the U.S. Department of Energy, Office of Science, Basic Energy Sciences, Materials Science and Engineering Division. This research used resources of the Advanced Photon Source, a U.S. Department of Energy (DOE) Office of Science User Facility operated for the U.S. DOE Office of Science by Argonne National Laboratory under Contract No. DE-AC02-06CH11357.

APPENDIX A: AN OPTIMIZATION-BASED APPROACH TO THE FOURIER-SPACE CONSTRAINT

Iterative schemes for phase retrieval alternate between updating an initial guess object between constraints in real and Fourier space. The Fourier-space iteration typically involves comparison with some form of measured data, such as a pixelated signal on an area detector. The update expression for the Fourier-space constraint is nonlinear and is arrived at by optimizing over one of many possible noise models associated with the measured data [22]. In this section, we adopt this general approach to derive (4) more rigorously.

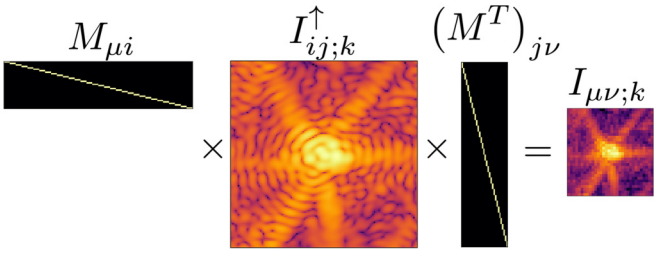


FIG. 7. Visualization of the binning operation in (A2) in matrix for $\alpha = 4$. Here, $i, j = 1, 2, 3, \ldots, 128$ and $\mu, \nu = 1, 2, 3, \ldots, 32$.

Given a well-sampled image of size $N \times N$ pixels from an image stack of size $N \times N \times N_2$ and a binning factor of α, we define the binning matrix M of size $(N/\alpha) \times N$ as

$$M_{\mu i} = \begin{cases} 1 & \text{if } (\mu - 1)\alpha < i \leqslant \mu\alpha \\ 0 & \text{otherwise.} \end{cases} \tag{A1}$$

For the kth low-resolution pattern $\mathbf{I}_k$ in the sequence of diffraction images, the binning operation in (1) is neatly expressed as the following double summation:

$$\begin{aligned} \langle I_{\mu\nu;k} \rangle &= \sum_{i=1}^{N} \sum_{j=1}^{N} M_{\mu i} \psi_{ij;k} \psi^*_{ij;k} (M^T)_{j\nu} \\ &= \sum_{i} \sum_{j} M_{\mu i} \psi_{ij;k} \psi^*_{ij;k} M_{\nu j}, \end{aligned} \tag{A2}$$

where we have used the fact that $I^{\uparrow}_{ij;k} = \psi_{ij;k} \psi^*_{ij;k}$ and assumed negligible background scattering. The binning is visualized in Fig. 7 as a matrix operation.

Keeping in mind that the noise associated with $I_{\mu\nu;k}$ is Poisson dominated in a physical measurement, we focus our mathematical treatment on the variance-stabilized random variable $\sqrt{I_{\mu\nu;k}}$ as described in Ref. [22]. The negative log-likelihood function for a measured dataset $I_{\mu\nu;k}$ resulting from a complex wave $\psi_{ij;k}$ in the far field is given by

$$\mathcal{L}[\boldsymbol{\psi}] = \sum_{k=1}^{N_2} \sum_{\mu=1}^{N/\alpha} \sum_{\nu=1}^{N/\alpha} \left[I^{1/2}_{\mu\nu;k} - \langle I_{\mu\nu;k} \rangle^{1/2} \right]^2. \tag{A3}$$

For some (i, j), the Wirtinger derivative [32] of $\mathcal{L}$ with respect to $\psi^*_{ij;k}$ is given by

$$\delta\mathcal{L} = \sum_{\mu,\nu,k} \left[1 - \left(\frac{I_{\mu\nu;k}}{\langle I_{\mu\nu;k} \rangle} \right)^{1/2} \right] \psi_{ij;k} \quad \forall i, j. \tag{A4}$$

Optimality dictates that the gradient above vanishes for the wave field $\boldsymbol{\psi} \equiv \hat{\boldsymbol{\psi}}$ that minimizes the fitting function in (A3). As a result, $\hat{\boldsymbol{\psi}}$ is the solution of the following set of nonlinear equations:

$$\hat{\psi}_{ij;k} - \left(\frac{I_{\mu\nu;k}}{\langle I_{\mu\nu;k} \rangle (\hat{\boldsymbol{\psi}})} \right)^{1/2} \hat{\psi}_{ij;k} = 0, \tag{A5}$$

where the dependency of the expected count $\langle I_{\mu\nu;k} \rangle$ on the unknown wave field $\hat{\boldsymbol{\psi}}$ is made explicit. Starting from an initial guess $\boldsymbol{\psi}^{(0)}$, the following fixed-point iteration is then usually employed to numerically solve (A5):

$$\psi^{(n+1)}_{ij;k} = \left(\frac{I_{\mu\nu;k}}{\langle I_{\mu\nu;k} \rangle (\boldsymbol{\psi}^{(n)})} \right)^{1/2} \psi^{(n)}_{ij;k} \quad \forall i, j, k. \tag{A6}$$

This is identical to (4) and the original version in Ref. [14], with the binning expressed using (A2). While we have derived the iteration step above for an error model designed to be robust to Poisson noise, the same mathematical treatment can be applied to different models, each of which would require optimization of an objective function different from (A3). See Ref. [22] for details.

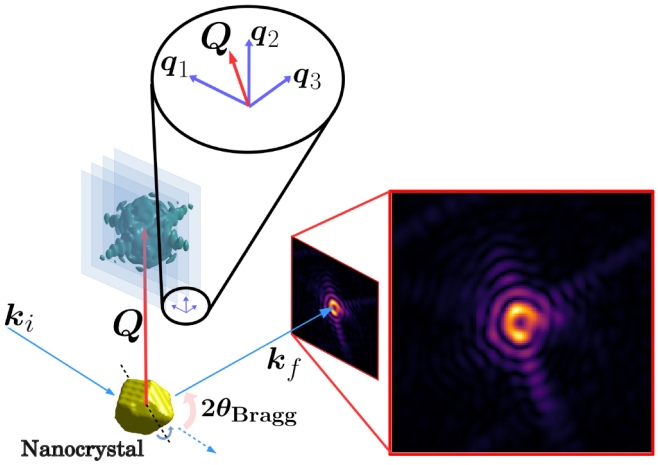


FIG. 8. BCDI schematic showing the three vectors $\boldsymbol{q}_1$, $\boldsymbol{q}_2$, and $\boldsymbol{q}_3$ along which Fourier space is being sampled. The zoomed-in region also shows the direction of $\boldsymbol{Q}$ in relation to these vectors. Here, $\boldsymbol{q}_1$ and $\boldsymbol{q}_2$ are mutually perpendicular and in the imaging plane (owing to the Cartesian pixel grid), while $\boldsymbol{q}_3$ is determined by the direction of change of $\boldsymbol{Q}$ in the rotating crystal experiment.

APPENDIX B: CROSSTALK BETWEEN SUCCESSIVE IMAGES IN HIGH-ENERGY BCDI

Figure 8 shows the Fourier-space sampling basis vectors $\boldsymbol{q}_1, \boldsymbol{q}_2, \boldsymbol{q}_3$ in a BCDI measurement. $\boldsymbol{q}_1$ and $\boldsymbol{q}_2$ are the mutually perpendicular sampling vectors in the imaging plane of the detector. $\boldsymbol{q}_3$ is determined by the change in the reciprocal lattice vector $\boldsymbol{Q}$ on account of the crystal rotation between two successive detector images: $\boldsymbol{q}_3 = -\delta\boldsymbol{Q}$. For most experimentally convenient combinations of Bragg scattering geometry, detector orientation, and direction of crystal rotation, $\boldsymbol{q}_3$ is not perpendicular to $\boldsymbol{q}_1$ and $\boldsymbol{q}_2$, implying a nonzero projection of $\boldsymbol{q}_3$ into the imaging plane. Therefore some crosstalk usually exists between the successive images collected in a BCDI measurement. If the detector plane is perpendicular to the exit beam, it can be shown that the angle between $\boldsymbol{Q}$ and the $\{\boldsymbol{q}_1, \boldsymbol{q}_2\}$ imaging plane is θ_{Bragg}, the Bragg angle which drops to below 3° for beam energies above 50 keV. Any meaningful rotation of the crystal at this beam energy or higher would leave a very small projection of $\boldsymbol{q}_3$ in the imaging plane, causing minimal crosstalk and therefore minimum sharing of information between successive acquired detector images.

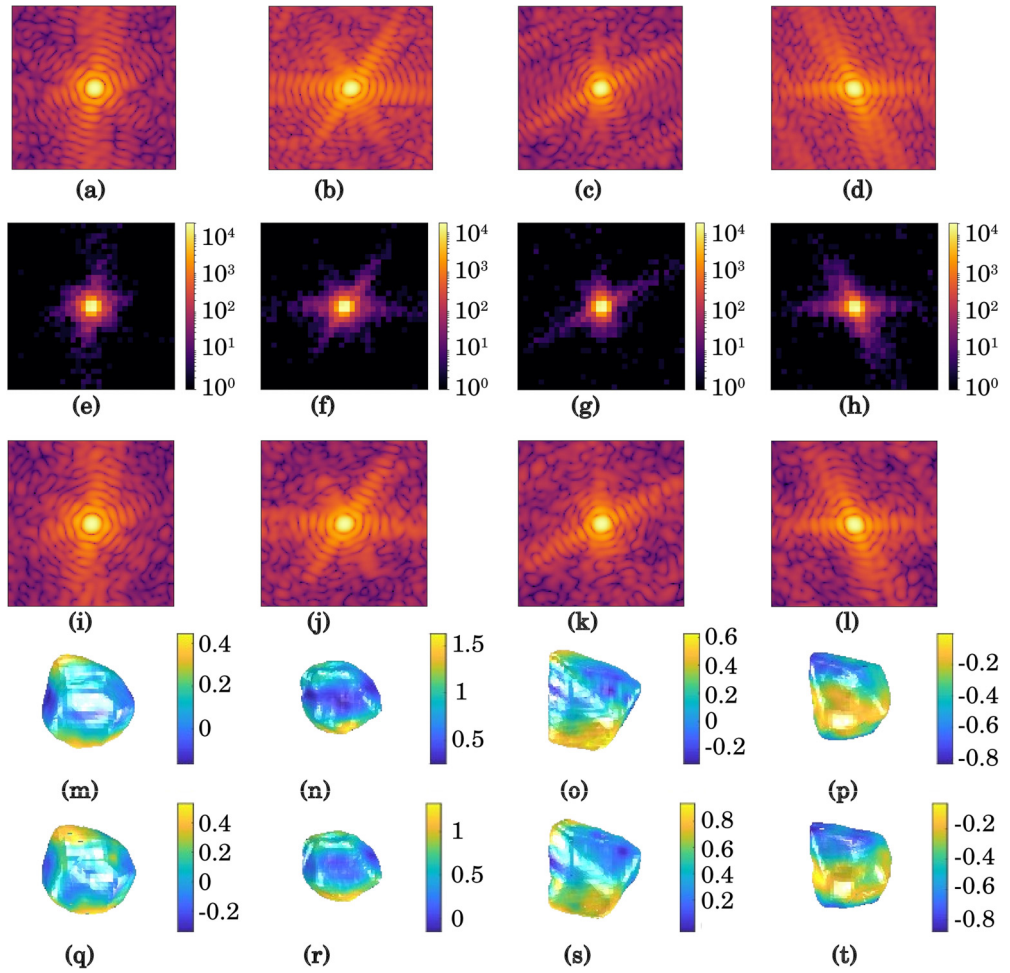


FIG. 9. (a)–(d) Central slices through diffraction signals corresponding to four different simulated complex scatterers (noise-free, well-resolved fringes with sampling rate $\sigma \simeq 5.8$ in the detector plane). (e)–(h) Central slices through the binned and noisy diffraction signals ($\alpha = 4$, sampling rate $\sigma \leqslant 1.6$). (i)–(l) Central slices through the diffraction signal recovered using the modified phase retrieval. (m)–(p) Isosurface plots of the scatterers recovered from the noisy binned signal, colored by phase (radians). (q)–(t) Isosurface plots of the scatterers recovered from the original well-resolved signal (a)–(d) with added Poisson noise. The conventional phase-retrieval recipe to obtain images (q)–(t) was 150 iterations ER + 100 iterations HIO + 250 iterations ER, with shrinkwrap every 50 iterations. The modified phase-retrieval recipe to obtain images (m)–(p) was 1500 iterations modified ER + 1500 iterations modified HIO + 2100 iterations modified ER, with shrinkwrap every 300 iterations.

APPENDIX C: ADDITIONAL RECONSTRUCTION RESULTS FOR VARIOUS FACETED SCATTERERS

Figure 9 shows the phase-retrieval results with the modified Fourier-space constraint, applied to the simulated coherent diffraction signals from four different particles, the size of each being $\simeq 22$ pixels in each dimension (smallest span was 20 pixels) and simulated on a $128 \times 128 \times 70$-pixel grid. The choice of $\alpha = 4$ for this array size resulted by design in poor fringe visibility, as we can see by computing the maximum effective sampling rate in the imaging plane: $\sigma = 128/(4 \times 20) = 1.6$, which is below the Nyquist rate of 2.

Also provided in Fig. 10 are the results of our algorithm applied to diffraction data manipulated in different ways. Figure 10(a) shows the results of our algorithm applied to the experimental data collected at a distance of 1.5 m (described in Sec. III C), after it has been binned in-plane at $\alpha = 3$. This is to be compared with the reconstruction in Fig. 6(b),

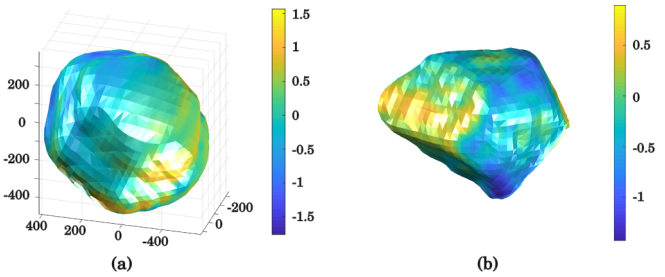


FIG. 10. (a) Isosurface plot of the reconstructed nanoparticle from Sec. III C, obtained from first taking the measured data at distance 1.5 m and binning it at $\alpha = 3$. The axes have dimensions of nanometers. (b) Isosurface of the reconstruction result from our algorithm, applied to the diffraction pattern from the synthetic particle in Fig. 3 that has been undersampled by a factor of 6 (i.e., every sixth pixel is chosen).

in which the same binning was achieved by translating the detector closer to the scatterer. While there is agreement between Figs. 10(a) and 6(b) with respect to the morphology of the crystal, we speculate that the slight differences in phase arise from the effects of binning the Poisson noise in addition to the signal itself.

Figure 10(b) shows the results of our algorithm applied to a truly undersampled data set, namely, from the synthetic particle shown in Fig. 3(a). The simulated diffraction pattern from this particle was undersampled by a factor of 6 (i.e., every sixth pixel was selected in both in-plane directions) and our phase-retrieval algorithm was applied to it with $\alpha = 6$. This treatment effectively assumes that the diffraction thus obtained has been binned and not undersampled. This result is to be compared with the reconstruction in Fig. 3(l), which was obtained from simulated diffraction binned at $\alpha = 6$. We see that while the morphology is faithfully reproduced, there are errors in the obtained phase. This can again be understood from the fundamental difference between sampling and binning as different mathematical transformations applied to the simulated diffraction, as we have mentioned in Sec. III A.

[1] J. R. Fienup, J. Opt. Soc. Am. A **4**, 118 (1987).
[2] I. K. Robinson, I. A. Vartanyants, G. J. Williams, M. A. Pfeifer, and J. A. Pitney, Phys. Rev. Lett. **87**, 195505 (2001).
[3] I. Robinson and R. Harder, Nat. Mater. **8**, 291 (2009).
[4] S. Hruszkewycz, M. Holt, C. Murray, J. Bruley, J. Holt, A. Tripathi, O. Shpyrko, I. McNulty, M. Highland, and P. Fuoss, Nano Lett. **12**, 5148 (2012).
[5] M. O. Hill, I. Calvo-Almazan, M. Allain, M. V. Holt, A. Ulvestad, J. Treu, G. Koblmuller, C. Huang, X. Huang, H. Yan *et al.*, Nano Lett. **18**, 811 (2018).
[6] W. Hu, X. Huang, and H. Yan, J. Appl. Crystallogr. **51**, 167 (2018).
[7] W. Ludwig, S. Schmidt, E. M. Lauridsen, and H. F. Poulsen, J. Appl. Crystallogr. **41**, 302 (2008).
[8] R. M. Suter, C. M. Hefferan, S. F. Li, D. Hennessy, C. Xiao, U. Lienert, and B. Tieman, J. Eng. Mater. Technol. **130**, 021007 (2008).
[9] J. V. Bernier, N. R. Barton, U. Lienert, and M. P. Miller, J. Strain Anal. Eng. Des. **46**, 527 (2011).
[10] M. Eriksson, J. F. van der Veen, and C. Quitmann, J. Synchrotron Radiat. **21**, 837 (2014).
[11] Y. Chushkin and F. Zontone, J. Appl. Crystallogr. **46**, 319 (2013).
[12] S. Maddali, I. Calvo-Almazan, J. Almer, P. Kenesei, J.-S. Park, R. Harder, Y. Nashed, and S. O. Hruszkewycz, Sci. Rep. **8**, 4959 (2018).
[13] A. F. Pedersen, V. Chamard, and H. F. Poulsen, Opt. Express **26**, 23411 (2018).
[14] D. J. Batey, T. B. Edo, C. Rau, U. Wagner, Z. D. Pešić, T. A. Waigh, and J. M. Rodenburg, Phys. Rev. A **89**, 043812 (2014).
[15] H. Özturk, X. Huang, H. Yan, I. K. Robinson, I. C. Noyan, and Y. S. Chu, New J. Phys. **19**, 103001 (2017).
[16] J. Goodman, *Introduction to Fourier Optics*, McGraw-Hill Physical and Quantum Electronics Series (W. H. Freeman and Company, New York, NY, 2005).
[17] S. Marchesini, Rev. Sci. Instrum. **78**, 011301 (2007).
[18] R. W. Gerchberg, Optik **35**, 237 (1972).
[19] S. Marchesini, H. He, H. N. Chapman, S. P. Hau-Riege, A. Noy, M. R. Howells, U. Weierstall, and J. C. H. Spence, Phys. Rev. B **68**, 140101(R) (2003).
[20] M. Odstrčil, M. Holler, and M. Guizar-Sicairos, Opt. Express **26**, 12585 (2018).
[21] P. Thibault and M. Guizar-Sicairos, New J. Phys. **14**, 063004 (2012).
[22] P. Godard, M. Allain, V. Chamard, and J. Rodenburg, Opt. Express **20**, 25914 (2012).
[23] A. Yau, W. Cha, M. W. Kanan, G. B. Stephenson, and A. Ulvestad, Science **356**, 739 (2017).
[24] J. Clark, X. Huang, R. Harder, and I. Robinson, Nat. Commun. **3**, 993 (2012).
[25] A. Ulvestad, Y. Nashed, G. Beutier, M. Verdier, S. O. Hruszkewycz, and M. Dupraz, Sci. Rep. **7**, 9920 (2017).
[26] D. Y. Noh, C. Kim, Y. Kim, and C. Song, J. Phys.: Condens. Matter **28**, 493001 (2016).
[27] J. C. Da Silva, A. Pacureanu, Y. Yang, S. Bohic, C. Morawe, R. Barrett, and P. Cloetens, Optica **4**, 492 (2017).
[28] C. Q. Tran, A. G. Peele, A. Roberts, K. A. Nugent, D. Paterson, and I. McNulty, Opt. Lett. **30**, 204 (2005).
[29] J. N. Clark and A. G. Peele, Appl. Phys. Lett. **99**, 154103 (2011).
[30] L. W. Whitehead, G. J. Williams, H. M. Quiney, D. J. Vine, R. A. Dilanian, S. Flewett, K. A. Nugent, A. G. Peele, E. Balaur, and I. McNulty, Phys. Rev. Lett. **103**, 243902 (2009).
[31] H. M. Quiney and K. A. Nugent, Nat. Phys. **7**, 142 (2011).
[32] L. Sorber, M. V. Barel, and L. D. Lathauwer, SIAM J. Optim. **22**, 879 (2012).